Calcium flux through ER-TGN contact sites facilitates cargo export

Running title: Secretory cargo sorting requires Ca^{2+} flux in ER/TGN contact sites

Bulat R. Ramazanov[1]†, Rosaria Di Martino[2]†, Abhishek Kumar[3], Anup Parchure[1], Yeongho Kim[1], Oliver Griesbeck[4], Martin A. Schwartz[1,3,5], Alberto Luini[2]†, Julia von Blume[1]†*

[1]Department of Cell Biology, Yale University School of Medicine, New Haven, CT

[2] Institute of Biochemistry and Cell Biology, National Research Council, Via Pietro Castellino 111, 80131 Naples, Italy

[3]Yale Cardiovascular Research Center, Cardiovascular Yale School of Medicine, Yale University,

[4] Max Planck Institute of Neurobiology, Martinsried, Germany

[5] Department of Biomedical Engineering, Yale University, New Haven, CT

† Authors have contributed equally to the work

*Corresponding author

Julia von Blume

333 Cedar Street

New Haven, CT 06510

USA

Yale email: julia.vonblume@yale.edu

Phone: +1 475 325 8124

Summary

The current study demonstrates the trafficking of Cab45 clients relies on Ca^{2+} flux between the endoplasmic reticulum (ER) and trans-Golgi Network (TGN). This process requires the activity of IP3 receptors, present in ER membranes, and depends on the integrity of the membrane contact site between these two organelles.

Abstract

Ca^{2+} influx into the trans-Golgi Network (TGN) promotes secretory cargo sorting by the Ca^{2+}-ATPase SPCA1 and the luminal Ca^{2+} binding protein Cab45. Cab45 oligomerizes upon a local Ca^{2+} influx, and Cab45 oligomers sequester and separate soluble secretory cargo from the bulk flow of proteins in the TGN. However, how this Ca^{2+} flux into the lumen of the TGN is achieved remains elusive, as the cytosol has a very low steady-state Ca^{2+} concentration. The TGN forms membrane contact sites (MCS) with the Endoplasmic Reticulum (ER), whereby the close apposition of the two organelles allows protein-mediated exchange of molecular species such as lipids. Here we show that TGN export of Cab45 clients requires the integrity of ER-TGN MCS and IP3R-dependent Ca^{2+} fluxes in the MCS, suggesting Ca^{2+} transfer between these organelles. Using a MCS targeted Ca^{2+} FRET sensor module, we measure the Ca^{2+} flow in these sites in real-time. These data show for the first time that ER-TGN MCS facilitate Ca^{2+} transfer required for SPCA1-dependent cargo sorting and export from the TGN and thus solves a fundamental question in cell biology.

67 ## Introduction

68 Protein secretion is a fundamental process and facilitates the integrity and cell-cell
69 communication of multiple-tissue organisms (Uhlen et al., 2015). Secreted proteins are
70 synthesized in the Endoplasmic Reticulum (ER) and transported to the Golgi apparatus in COPII
71 coated vesicle (Barlowe and Miller, 2013; Gillon et al., 2012; Zanetti et al., 2013). Upon reaching
72 the Golgi apparatus, these cargo molecules further transit from the *cis* to *trans* Golgi cisterna and
73 finally reach trans Golgi Network (TGN) (De Matteis and Luini, 2008; Di Martino et al., 2019;
74 Ford et al., 2021; Guo et al., 2014; Kienzle and von Blume, 2014). Protein transport between
75 Golgi cisternae and towards the TGN is still highly debated and several models have been
76 proposed (Dunlop et al., 2017; Dunphy and Rothman, 1985; Glick et al., 1997; Glick and Luini,
77 2011; Glick and Nakano, 2009; Lujan and Campelo, 2021; Nakano and Luini, 2010). At the
78 TGN, these proteins are sorted and packed into different transport carriers to reach their
79 destination such as the cell surface, the endosomal system, or secretory granules in specialized
80 cells (Mostov and Cardone, 1995; Stalder and Gershlick, 2020; Tang, 2001).

81 Protein sorting at the TGN is a complex process involving physical features of the cargoes
82 themselves and elements of the local environment and so remains a poorly understood process
83 for many proteins. Understanding how soluble secretory proteins can be accurately and
84 specifically sorted to the plasma membrane is a particular challenge. There are no cargo receptors
85 that connect these soluble molecules to the TGN membrane (Kienzle and von Blume, 2014;
86 Pakdel and von Blume, 2018; Ramazanov et al., 2021).

87 Our work and others have shown that Calcium (Ca^{2+}) is a major regulator of cargo sorting
88 at the TGN. Secretory Pathway ATPase 1 (SPCA1) pumps Ca^{2+} from the cytoplasm into the
89 TGN lumen in an ATP-dependent manner (Kienzle et al., 2014; Lebreton et al., 2021; Lissandron

90 et al., 2010; Missiaen et al., 2007; Pizzo et al., 2011; Pizzo et al., 2010; Sepulveda et al., 2008;
91 von Blume et al., 2011; Wong et al., 2013). In response to luminal Ca^{2+} influxes, the Golgi
92 resident protein Cab45 oligomerizes and captures cargo molecules before they are packed into
93 sphingomyelin-rich vesicles that bud from the TGN (Crevenna et al., 2016; Deng et al., 2018;
94 Scherer et al., 1996; von Blume et al., 2012). Despite the importance of Ca^{2+} in these processes,
95 the source of the Ca^{2+} that is pumped into the TGN lumen by SPCA1 is unknown as the cytosolic
96 Ca^{2+} concentrations are limited to the low nanomolar scale (Berridge et al., 2003).

97 The TGN forms MCSs with the ER where lipids are transferred to mediate non-vesicular
98 inter organelle communication (Masone et al., 2019; Venditti et al., 2020; Venditti et al., 2019).
99 Endoplasmic reticulum to TGN membrane contact sites (ER-TGN MCSs) contain tethering
100 proteins such as vesicle-associated membrane proteins A and B (VAPA and VAPB) and lipid
101 transfer proteins such as Oxysterol-binding protein 1 (OSBP1) (Lehto and Olkkonen, 2003).
102 OSBP1 possesses dual organelle targeting motifs as it is able to bind the ER proteins VAPA and
103 VAPB through an acidic track (FFAT) domain, and it is also able to bind to the TGN through
104 Pleckstrin homology (PH) domain, which recognizes Phosphatidylinisitol-4-phosphate (PI4P) or
105 Arf1-GTP on TGN membrane (Kawano et al., 2006; Kumagai and Hanada, 2019; Mesmin et al.,
106 2017). At the ER/TGN interface, OSBP1 counter transports PI4P from the TGN and cholesterol
107 from the ER in a the process mediated by the oxysterol-binding domain (OBD) of OSBP1 that
108 binds PI4P or cholesterol in a mutually exclusive manner (Mesmin et al., 2013).

109 Recent studies report the importance of lipid transfer in ER-TGN MCSs in regulating
110 protein export from the TGN (Wakana et al., 2021). In addition to their implication in lipid transfer,
111 MCSs allow Ca^{2+} transfer between the ER and other organelles such as the mitochondria (Kelly,
112 1985; Pfeffer and Rothman, 1987; Rizzuto et al., 1993; Rizzuto et al., 1998). We therefore

113 hypothesized that ER-TGN MCSs could provide Ca^{2+} to facilitate SPCA1 and Cab45-dependent
114 cargo sorting at the TGN. Here we show that the trafficking of Cab45 clients relies on the IP3
115 receptor (IP3R), present in ER membranes, and on the integrity of the ER-TGN MCSs. We
116 generated a MCS specific sensor to measure Ca^{2+} flux within these sites, revealing that this Ca^{2+}
117 flux plays an essential role for cargo export from the TGN and is dependent on tethering between
118 ER and TGN. With these data we solve a major unresolved question in cell biology.
119

120 ## Results and discussion

121 ***Inhibition of IP3R delays TGN export of Cab45 clients***

122 Our previous work demonstrates that sorting soluble secretory proteins requires a transient
123 SPCA1-mediated Ca^{2+} influx into the TGN to facilitate Cab45 oligomerization (Crevenna et al.,
124 2016; Deng et al., 2018; von Blume et al., 2012). The cytosolic Ca^{2+} concentrations at steady state
125 are in the low nanomolar range thus may not provide the amount of Ca^{2+} ions required to promote
126 sorting of Cab45 clients (Crevenna et al., 2016; Pizzo et al., 2011). Therefore, we hypothesized
127 that with the established MCS between the ER and the TGN, and the ER being the largest Ca^{2+}
128 store within the cell, it is a likely candidate to provide Ca^{2+} for sorting at TGN, and this process
129 could be mediated through an IP3 receptor (IP3R)-dependent mechanism.

130 To investigate if the release of Ca^{2+} from the ER has an impact on the sorting and export
131 of soluble secretory cargo molecules from at TGN, we analyzed trafficking and secretion of the
132 well-established Cab45-clients: cartilage oligomeric protein (COMP) and Lysozyme C (LyzC)
133 (von Blume 2011; von Blume 2012) in the presence and absence of the IP3R antagonist (2-APB)
134 (Maruyama et al., 1997). We used the retention using selective hooks (RUSH) system to quantify
135 the trafficking and packaging of COMP or LyzC, respectively, into secretory vesicles in HeLa
136 cells in the presence of 2-APB (70 μM) or DMSO (control) (Boncompain et al., 2012). To this
137 end, HeLa cell lines were transfected with RUSH-constructs containing COMP-EGFP or LyzC-
138 EGFP to analyze intracellular trafficking of EGFP-fused proteins at different time points after
139 synchronous release from the ER by biotin addition (**Figure 1A**). We observed simultaneous
140 export of COMP-EGFP from the ER in control and 2-APB treated cells (**Figure 1B [0, 20 min]**).
141 However, the appearance of cytosolic vesicles (TGN carriers) was significantly delayed in cells
142 treated with 2-APB compared to control cells at later time points (**Figure 1B, C [30, 40, 60 min]**).

143 To confirm the observed phenotype on a cell population, we performed RUSH experiments
144 using COMP-EGFP as cargo in HeLa line treated with DMSO (control) or 2-APB with subsequent
145 FACS analysis. We used this assay to quantify the intracellular accumulation of EGFP-COMP in
146 DMSO or 2-APB treated cells. Cells were fixed at 0, 30, 60 and 120 min after biotin addition and
147 10^4 cells for each time-point were analyzed by FACS. We calculated the average arithmetical value
148 for fluorescent intensity of COMP-EGFP obtained from the FL-1 channel for each sample. The
149 arithmetical average values for fluorescence intensity of COMP-EGFP from 2-APB treated cells
150 were 1.8 and 2.1-fold higher than in control cells after 60 and 120 minutes after biotin addition,
151 respectively, indicating a longer residence of the EGFP-COMP inside cells in 2-APB treated cells
152 confirming our microscopy observations (**Figure 1D, Supplementary S1A, S1C**).
153 To correlate these results with the actual TGN exit of the cargo molecules, we applied live-
154 cell imaging of the exiting EGFP-tagged cargo molecules in the presence of the GALNT1-BFP
155 TGN marker. We measured time-dependent changes in fluorescence intensity of EGFP-tagged
156 protein within ROI of TGN defined by the GALNT1-BFP signal. These results showed that the
157 reduction in the number of vesicles in 2-APB treated cells in the RUSH experiments was consistent
158 with prolonged residence of cargo in the TGN compared to DMSO treated cells (**Figure 1E**). To
159 quantify this phenotype, we applied a non-linear regression function of the intensity values on the
160 plot shown on Figure 1D (**Supplementary S1E**). In addition, we calculated span values for each
161 curve representing changes of LyzC-EGFP intensity within Golgi ROI. The span was defined as
162 the difference between the fluorescence intensity of EGFP at the starting point and predicted
163 plateau for each curve, representing a change in fluorescence intensity during the experiment. The
164 span value calculated for LyzC-EGFP expressing cells in the presence of 2-APB exhibited a two-

165 fold decrease compared to control cells (span value for 2-APB and DMSO samples were 0.8 and
166 1.5 respectively), indicating a significant defect in TGN export of LyzC-EGFP in these cells.

167 To further validate that inhibition of IP3R reduces secretion of Cab45 client LyzC from the
168 cells, we performed a secretion assay. We generated stable cell lines expressing EGFP tagged
169 LyzC under a constitutive promoter by lentiviral transduction of HeLa cells. Secretion assays were
170 performed in a complete growth medium, and secreted LyzC-EGFP in the supernatant was
171 immunoprecipitated using GFP trap agarose beads prior to analysis by western blotting. The
172 western blot analysis revealed a 48% reduction in secretion LyzC-EGFP into the cell culture media
173 in 2-APB treated condition compared to DMSO treated control cells (**Figure 1F**).

174 These data suggested that the activity of IP3 receptors impacts the TGN export and
175 secretion of Cab45-clients. Previous work has shown that Golgi localized IP3 receptors have no
176 impact on SPCA1 dependent Ca^{2+} uptake (Wong et al., 2013), therefore we speculated that Ca^{2+}
177 flow between these organelles might be facilitated by ER-TGN MCS (Ramazanov et al., 2021).

178

179 ***MCS integrity is essential for TGN export of Cab45 clients***

180 VAPA and VAPB proteins play an essential role in maintaining ER-TGN MCS integrity
181 by tethering ER and TGN. Deleting these proteins from cells leads to a reduction of contacts
182 between the organelles (Lev, 2010; Phillips and Voeltz, 2016). To examine the role of the integrity
183 of the ER-TGN contact sites on trafficking of Cab45-clients, we performed RUSH experiments,
184 and we analyzed the trafficking of COMP-EGFP in VAPA/VAPB depleted HeLa cells. To this
185 end, HeLa cells were transfected with non-targeting siRNA as control or siRNAs targeting VAPA
186 and VAPB. After 24 hours, HeLa cell lines were transfected with RUSH-constructs expressing
187 COMP-EGFP. RUSH experiments were performed, and samples were fixed after different

188 timepoints of biotin addition. Immunofluorescence images captured at 30, 40, and 60 minutes after
189 biotin addition showed that compared to control cells, VAPA/VAPB siRNA treated cells exhibited
190 a significant delay in the formation of COMP-EGFP containing post-Golgi vesicles (**Figure 2A**
191 **[30, 40, 60 min]**). Consistent with this result, quantification of post-Golgi vesicles after different
192 time points from a randomly selected population of control siRNA or VAPA/VAPB siRNA treated
193 cells revealed a decrease in the amount of TGN derived vesicles (**Figure 2B**).

194 We confirmed the phenotype of delayed export of Cab45 clients seen in VAPA and VAPB
195 knockdown with RUSH LyzC or COMP, respectively, in control versus VAPA/VAPB-dKO HeLa
196 cell lines (Dong et al., 2016) (see immunofluorescence **Supplementary S2A, S2B [0, 20 min]**),
197 and quantification (**Supplementary S2C, S2D**). In parallel, we measured time-dependent
198 intracellular decrease of COMP-EGFP by FACS in control versus VAPA/VAPB deficient cells.
199 The average intensity values in the GFP channel from VAPA and VAPB deficient cells were 1.5-
200 fold higher than in control cells at the 60 and 120 minutes after biotin addition, indicating
201 accumulation of COMP-EGFP in these cells (**Figure 2C, Supplementary S1A, S1C**).

202 To demonstrate that the secretion defect is caused by impaired TGN export we performed
203 live-cell imaging of the exiting EGFP-tagged Cab45 clients in the presence of the GALNT1-BFP
204 TGN marker. We observed time-dependent changes of LyzC-EGFP intensity within the TGN ROI
205 and a 1.6-fold difference in span values in control versus VAPA and VAPB depleted cells. In
206 addition, we observed a prolonged residence of LyzC in the TGN of HeLa cell lines transfected
207 with siRNA to VAPA and VAPB compared control cells (**Figure 2D, Supplementary S1F**). The
208 efficiency of knockdowns of VAPA and VAPB proteins were analyzed by western blotting
209 (**Figure 2E**).

210 To investigate that this phenotype is specific for certain secretory soluble proteins and does
211 not affect other proteins that are transported by bulk flow secretion, we measured the time-
212 dependent intracellular decrease of COMP-EGFP and EQ-sol-GFP by FACS in control versus
213 VAPA/VAPB deficient HeLa cells as well as 2-APB treated cells. These data indicated that the
214 secretion of EQ-sol, non-specific bulk flow secretion marker, representing soluble non-toxic
215 version of equinatoxin II-based reporter EQ-SM (Deng et al., 2016), is unaffected in VAPA and
216 VAPB-depleted HeLa line compared to WT cell line (**Suppl. S1A-C**).
217 Together these data showed that the TGN export of the Cab45 clients COMP and LyzC
218 from TGN requires intact MCSs between ER and TGN (**Figure 2**) and IP3R-dependent Ca^{2+}
219 release from the ER (**Figure 1**). These data also suggested that ER-TGN MCS could serve as
220 potential sites for Ca^{2+} transfer.
221
222 ***Targeting Twitch based FRET sensors to ER-TGN MCS***
223 Our next goal was to directly test potential Ca^{2+} flow at ER-TGN MCSs. We hypothesized
224 that these MCSs would be potential structures that could serve as hotspots for Ca^{2+} transfer
225 between the organelles. To evaluate possible Ca^{2+} flows in these sites, we used Förster resonance
226 energy transfer (FRET)-based Ca^{2+} biosensors called Twitch. These sensors contain a minimal
227 Ca^{2+} binding moiety derived from the C-terminal domain of troponin C incorporated between
228 mCerulean3 and cpVenuscd (Thestrup et al., 2014). To target the sensors to ER-TGN MCS in
229 living cells, we introduced an amino acid sequence coding the N-terminal region of OSBP1 that
230 includes a PH and an FFAT motif (**Figure 3A**). As the N-terminal disordered domain of OSBP
231 seems to be crucial for active lipid transport in the ER-TGN MCS (Jamecna et al., 2019), we
232 generated sensors containing disordered domain (N-PH-FFAT) as well as sensor without that

233 domain (PH-FFAT) (**Supplementary S3A, S3B**). To obtain stable and equal protein expression
234 levels, we constructed stable HeLa cell lines expressing the MCS-Twitch sensors under a
235 doxycycline-inducible promoter. We confirmed the expression of the respective sensor after
236 doxycycline induction by immunofluorescence and live-cell imaging (**Supplementary S3B**). To
237 investigate the correct localization of the sensors at the TGN, cells were fixed and stained with
238 antibodies recognizing against GM130 or TGN46. The immunofluorescence microscopy data
239 confirmed that the MCS-Twitch sensors expressed in HeLa cells correctly localize
240 (**Supplementary S3C, S3D**).
241
242 ***The Twitch2b-MCS FRET sensor detects Ca^{2+} flows***
243 To determine the range of Ca^{2+} signals detectable at the MCS at steady-state (non-treated
244 cells incubated at 37°C), we constructed four MCS-Twitch sensors with different Ca^{2+} affinities
245 (depicted in **Supplementary Tables 1, 2**). For quantitative FRET measurements of Ca^{2+}, we
246 calculated the FRET index value in the cell line expressing the respective sensor as an
247 approximation of the FRET/molecule (Grashoff et al., 2010; Kumar et al., 2016). The acquisition
248 of the normalized FRET index values was obtained by measuring FRET intensity, subtracting the
249 background noise and the bleed-through for the two fluorophores, and normalizing to FRET
250 acceptor intensity. Measuring FRET indexes from the MCS-Twitch sensors at steady revealed that
251 compared to MCS-Twitch9x, MCS-Twitch7x, MCS-Twitch8x, the Twitch2b sensor showed the
252 highest FRET index (**Supplementary S3E**).
253 To test if the Twitch2b sensor was responsive to Ca^{2+} perturbations in the cells, we
254 performed a series of control experiments. First, we determined the FRET values in HeLa cells
255 expressing the respective MCS-Twitch sensor by live-cell fluorescence microscopy in cells treated

256 with DMSO (control) or the Ca^{2+} chelating agent BAPTA-AM. As expected, chelating
257 intracellular Ca^{2+} ions with BAPTA-AM, showed a significant decrease in the FRET index of
258 MCS-Twitch2b (**Figure 3E, F**). The FRET indices of MCS-Twitch2b upon treating the cells with
259 BAPTA were similar to the baseline levels of the low Ca^{2+} affinity MCS-Twitch7x, 8x and 9x
260 sensors (**Figure C, D; Supplementary S3E**). Therefore, Twitch2b was selected for all further
261 experiments.

262 To quantify the range of free Ca^{2+} concentrations, we calibrated the Twitch2b sensor. To
263 calibrate Twitch2b in live cells, we used HeLa cells stably expressing CYTO-Twitch2b. We
264 applied a reciprocal dilution of buffers containing increasing ratios of Ca-EGTA/K2-EGTA
265 concentrations, and the free Ca^{2+} ion concentrations were calculated as described in Materials and
266 Methods (**Supplementary S4A, S4B**). The FRET indexes obtained from Twitch2b at different
267 ratios of Ca-EGTA/K2-EGTA in the calibration experiment allowed us to build a calibration curve
268 and which demonstrated a strong correlation between the FRET index value and the concentration
269 of free Ca^{2+} (calibration plot shown in **Figure 3B**). Thus, we developed a powerful tool to measure
270 Ca^{2+} levels in the ER-TGN-MCS. The calibration experiment allowed us to calculate the Ca^{2+}
271 levels at the MCS based on FRET indices.

272 To measure increased intracellular Ca^{2+} concentrations on the FRET signals from MCS-
273 Twitch2b sensors, we utilized active and passive means of increasing cytosolic Ca^{2+} levels.
274 Treatment of cells with ionomycin, that raises the intracellular Ca^{2+} level caused a significant
275 increase in the FRET index (**Figure 3G, H**). Several signaling pathways, including cell surface
276 receptors, are known to utilize Ca^{2+} ions as secondary messengers for downstream signaling
277 (Carafoli, 2002; Dickenson and Hill, 1994; Thillaiappan et al., 2017). Activation of Histamine
278 receptors (H1-receptor) at the plasma membrane causes the activation of PLC, which in turn

279 elevates intracellular Ca^{2+} through an IP3-dependent mechanism. To test if MCS sensor detects
280 these signals, we performed the FRET measurements in HeLa cells expressing PH-FFAT-
281 Twitch2b incubated with either DMSO (control) or after treatment with histamine. (**Figure 3I, J**).
282 The data clearly showed an increase in the FRET index– revealing a profound, physiological link
283 between MCS Ca^{2+} levels and the signaling receptor IP3.

284 Because we did not observe difference in the FRET index values between PH-FFAT-
285 Twitch and N-PH-FFAT-Twitch sensors (**Supplementary 3E, 3F, 3G, 3H**), we decided to
286 perform further experiments by using the PH-FFAT targeting motif.

287 The data indicates that release of Ca^{2+} caused by IP3R stimulation leads to an increase in
288 Ca^{2+} levels in MCS and our sensor precisely measures these changes.

289

290 ***TGN protein abundance and Ca^{2+} flux at MCS are coupled***

291 Our former work has shown that TGN Ca^{2+} influx is necessary for the TGN exit of
292 secretory proteins (Crevenna et al., 2016; Deng et al., 2018; Kienzle et al., 2014; von Blume et
293 al., 2011). Therefore, we hypothesized that there must be a correlation between cargo influx into
294 the TGN and Ca^{2+} flow in the MCS. To test if Ca^{2+} in ER-TGN MCSs is influenced by protein
295 abundance, we treated HeLa cells expressing MCS-Twitch 2b with Cycloheximide (CHX), that
296 blocks protein synthesis. We incubated cells for 1, 2 and 4 hours and analyzed FRET signals.
297 Analyzing the FRET data showed a time-dependent decrease in the FRET index of cells treated
298 with CHX. To further demonstrate that this is correlated with cargo abundance in the TGN, we
299 incubated HeLa cells expressing MCS-Twitch 2b at 20°C to arrest secretory proteins in the TGN
300 (Ladinsky et al., 2002; Matlin and Simons, 1983). Notably, FRET values were significantly
301 decreased in cells incubated at 20°C (**Figure 4A, B**). Duration of the 20°C blocks for more than

302 1-hour did not affect the average FRET index values (**Figure 4C**). More importantly, incubation
303 of cells at 37°C after the 20°C-block resulted in a complete recovery of the FRET index (**Figure**
304 **4B, C)**. To validate that the changes in the FRET indices were not due to other factors, cells were
305 incubated at 37°C and 20°C in the presence of ionomycin (**Figure 4E**). Independent of the
306 incubation temperature, ionomycin treatment led to a recovery of FRET indexes demonstrating
307 that the effects are specific to Ca^{2+}. These data supported that the Ca^{2+} flux in the MCS is
308 stimulated by the presence of newly synthesized protein. Furthermore, we showed that this is
309 specific to the cargo abundance in the TGN.

310 In the current study, we quantify the abundance of Ca^{2+} flux in the ER-TGN MCS, which
311 has remained unknown. We also demonstrate that cargo entering the TGN elicits a Ca^{2+} release in
312 the MCS that is required for sorting Cab45 clients into a TGN-derived carrier (**Figure 5A**).

313 Our previous work has shown that SPCA1, the only Ca^{2+} ATPase in the TGN, is required
314 for secretory cargo sorting in the TGN (von Blume et al., 2011). Interestingly, these studies also
315 exemplified that the Ca^{2+} binding protein Cab45 oligomerizes and forms a scaffold for collecting
316 its clients, including LyzC and COMP (Crevenna et al., 2016; von Blume et al., 2012).
317 Furthermore, sphingomyelin produced by SMS1 promotes SPCA activity and Cab45/client export
318 from the TGN (Deng et al., 2018). However, the source of Ca^{2+} that drives the process has
319 remained unknown (Ramazanov et al., 2021). In the current work, we demonstrate that the TGN
320 export COMP and LyzC, require the integrity of ER-TGN MCS and IP3R-dependent Ca^{2+} fluxes
321 in the MCS, suggesting that Ca^{2+} transfer between these organelles is the primary source for
322 SPCA1.

323 The autoregulation of the secretory pathway by cellular signaling remains mysterious. However,
324 central principles have been uncovered in recent years (Di Martino et al., 2019). The signaling

325 pathway that stimulates the Ca^{2+} release through the contact site remains unknown. Our work
326 elucidates that it is directly linked to IP3 production and activation of IP3R in close proximity to
327 ER-TGN contact sites. Although current work provides an understanding of upstream signaling
328 events that regulate of sorting of soluble proteins at TGN and depend on the activity of SPCA1,
329 the possibility that LyzC and COMP themselves could serve as a stimulus for the activation of
330 such pathways remains to be investigated.
331

332 # Materials and methods

333 ## DNA techniques and plasmid construction

334 Restriction enzymes for molecular biology were obtained from New England Biolabs.
335 PCRs were performed with a Phusion Polymerase (Thermofisher) and a Mastercycler Nexus
336 (Eppendorf). All plasmids used in this study bear ampicillin resistance for selection in *Escherichia*
337 *coli* and are listed in Table 1, where the transgenes and inserts are described. The DNA sequences
338 encoding PH-FFAT/N-PH-FFAT domains of OSBP1 fused with Twitch sensors were integrated
339 into donor plasmid of the transposon-based piggyBac system for stable transgene-expressing cell
340 lines generation (Li et al., 2013). The piggyBac backbone vector (PB-T-PAF) and PB-RN and
341 PBase were a gift of James Rini, University of Toronto, Ontario, Canada (Li et al., 2013). In brief,
342 to generate PB-T-PAF-PHFFAT-Twitch constructs the PB-T-PAF vector was linearized with NheI
343 and NotI-HF restriction enzymes (NEB). PH-FFAT/N-PH-FFAT sequences (5'-NheI/3'-AscI)
344 were amplified by PCR from pLJM1-FLAG-GFP-OSBP plasmid (Addgene#134659). The
345 sequences encoding Twitch (Twitch2b/Twitch7x/Twitch8x/Twitch9x) Calcium sensors were
346 obtained from plasmids that have been generously provided from Oliver Griesbeck Lab and were
347 amplified by adding corresponding restriction sites (5'-AscI/3'-NotI). All fragments were ligated
348 in PB-T-PAF backbone. All cloning experiments were conducted using Phusion High-Fidelity
349 Polymerase and T4 ligase (Thermo Fisher Scientific) according to the manufacturer's instructions.
350 VAPA-Twitch2b and CYTO-Twitch2b constructs were generated by similar strategies. The
351 sequences encoding Twitch2b for these constructs were amplified by adding corresponding
352 restriction sites (5'-NheI/3'-AscI). The VAPA fragment was amplified from plasmid coding full
353 length VAPA protein and was gifted from Pietro De Camilli with addition of AscI and NotI
354 restriction sites. CYTO-Twitch2b construct was generated from VAPA-Twitch2b by replacing

355 VAPA sequence by short stop-codon containing fragment, annealed by using following sequences
356 (5'CGCGCCAGAGGAGTTTTAAGC3' and 5'GGCCGCTTAAAACTCCTCTGG3'). pLenti-
357 LyzC-EGFP for secretion assay lines was generated using gateway cloning reaction by amplifying
358 LyzC-EGFP from plpcx-LyzC-EGFP and cloning into pDONR221 using BP cloning reaction and
359 then subsequently using LR cloning reaction into the destination vector to generate the desired
360 construct. The correct sequence of all constructs was confirmed by DNA sequencing using the
361 SmartSeq Kit from Eurofins Genomics or KECK sequencing (Yale University).

362 **Cell culture and generation of stable cell lines expressing Calcium sensor constructs.**

363 Cell lines were maintained in DMEM media (Gibco) containing 10% FBS (Sigma
364 12306C-500ML) at 37°C and 5% CO_2. For transfection cells were plated in antibiotic-free media
365 24 hours before the procedure. DNA transfections were performed by using Lipofectamine 2000
366 reagent according to the manufacturer's protocol. After 8 hours the media was replaced. Transgene
367 expression was estimated at 48 hours after transfection. To generate cell lines stably expressing
368 the mentioned above transgenes HeLa lines were used. In brief, HeLa cells at 70% confluency
369 were transfected with PB-T-PAF (with corresponding transgene), PB-RN, and PBase (total DNA
370 1.5 µg; at ratio 8:1:1) using Lipofectamine 2000 in OptiMEM-I media. Cells were selected for 48
371 hours with 2 µg/ml puromycin dihydrochloride (Sigma-Aldrich) and for 7 days with 400 µg/ml
372 G418 disulfate salt (A1720-5G, Sigma-Aldrich). To induce transgene expression cells were
373 incubated in presence of doxycycline (J63805 Alfa Aesar, USA) (1ug/mL) for 24 hours. The
374 generated lines were sorted on BD FACS Aria to exclude resistant cells without transgene
375 expression.

376 HeLa cell lines stably expressing LyzC-EGFP were generated using lentiviral transduction
377 containing pLenti-LyzC-EGFP construct with followed Blasticidin 8 ug/mL (InvivoGen)

378 selection for 48 hours. siRNA transfections were performed using Lipofectamine RNAiMAX
379 according to standard protocol. VAPA/VAPB-dKO lines were generated by Pietro De Camilli Lab
380 and published previously (Dong et al., 2016).

381 **RUSH cargo sorting assay and fluorescent microscopy**

382 RUSH assay was performed as described previously (Boncompain et al., 2012; Deng et al.,
383 2018). Studied cell lines were cultured in 6-well plates (Cat#353046, Corning) on glass slides (Cat.
384 #72290-04, EMS) and transfected with RUSH-COMP-EGFP and RUSH-LyzC-EGFP constructs
385 using Lipofectamine 2000 according to standard protocol. At 24 hours post transfection, cells were
386 incubated with 40 µM d-Biotin (Sigma) ingrown media for different time points (20, 30, 40, 60,
387 and 90 min or without d-Biotin (control). For IF slides, cells were washed once with PBS, fixed in
388 4% PFA (Electron Microscopy Sciences) in PBS for 10 min, and mounted on 12mm coverslips
389 (Electron Microscopy Sciences) using ProLong Gold (Thermo Fisher Scientific). Nuclear
390 chromatin was stained by short incubation in 2.5uM DAPI (Biolegend) solution. Acquisition of
391 either GFP was performed by using a Delta Vision system by imaging z-stacks with a step size of
392 0.2 µm.

393 For quantification of vesicles, we empirically measured the sizes of objects between 4 and
394 20 pixels using the Analyze Particles function in ImageJ, which detects vesicular structures but
395 omits larger structures such as the Golgi. While small-fragmented and isolated Golgi structures
396 could be detected in error, such structures are rare. Furthermore, only vesicles of cells expressing
397 the RUSH construct were counted. The Fiji macro count_fixed_vesicles_V1.3 (M. Pakdel)
398 including the Particle Analyzer plug-in by Fiji was used to determine the number of vesicles (Deng
399 et al., 2018). Kruskal–Wallis one-way analysis of variance was used for comparisons in RUSH
400 experiments.

401 For immunostaining, cells were cultured in six wells on glass slides and fixed for 10 min
402 with 4% paraformaldehyde. After washing with PBS, cells were permeabilized for 5 min in 0.2%
403 Triton-X 100 and 0.5% SDS in 4% BSA. After washing with PBS, cells permeabilized with Triton-
404 X 100 were blocked with 4% BSA for 1 h. Cells were incubated with primary followed by
405 corresponding secondary antibody for 1 h at room temperature in blocking buffer in the dark.
406 Slides were washed three times with PBS after incubation with antibody. Glass slides were
407 mounted with ProLong Gold (Thermo Fisher Scientific). Antibodies to TGN46 (AHP500G,
408 Biorad) and GM130 (610822, BD) were used at dilution 1:200.
409 For FACS analysis cells were fixed with 4% PFA for 10 min. After fixation washed with
410 ice-cold DPBS and dissociated using trypsin-EDTA solution. Cells were washed with DPRS three
411 times by centrifugation at 200g for 5 min each. FACS analysis was performed using BD LSRII
412 machine. 10000 cells were analyzed for each sample. FACS data was analyzed using FlowJo
413 10.5.3 for Windows.
414
415 **RUSH protein trafficking analysis**
416 HeLa cells were seeded on Mattek dishes (p35gc-1.5-14-c, Mattek) and cultured at 37°C
417 with 5% CO_2. The next day or the day before imaging, cells were transfected by Lipofectamine
418 2000 (Invitrogen) with two plasmids expressing GalT-BFP (a trans-Golgi maker from James
419 Rothman lab) and RUSH COMP or RUSH Lysozyme C (see above for details of the plasmids).
420 After five to eight hours, cells were washed and incubated with DMEM with 10% FBS overnight.
421 Before imaging, cells were washed and briefly incubated with 37°C-warmed DMEM
422 supplemented with 10% FBS and HEPES buffer (Gibco, 21063029). Cells were then staged on the
423 microscope as described below.

424 Live-cell imaging was performed using a spinning disk confocal microscope CSUXfw-
425 06p-01 (Yokogawa) on Nikon eclipse Ti2 (LWD NA=0.52) microscope stand with a motorized
426 stage with stage top Piezo. sCMOS camera Photometrics Prim 95B and CFI Plan Apo Lambda
427 60x oil objective were used. Also, the Oko Lab temperature control system was set to 37°C and
428 the fluorescence (405 nm and 488 nm) was induced by using an Agilent laser combiner. Images
429 were acquired using Nikon Elements. Fluorescence images were taken every three minutes after
430 adding biotin (see above for the methods for RUSH experiments). At each time point, the Nikon
431 Elements stitched 6x5 fields to generate relatively large field images that could accommodate at
432 least 10 distinguished secretion events through 90 or 120 minutes.

433 The time-course images generated above were imported to Fiji (ImageJ). Images
434 containing individual cells with distinguishable Golgi and RUSH signals were cropped as stored
435 separately. The Golgi masks were generated by using GalT-BFP signals (405 nm excitation) and
436 ImageJ Auto-threshold and were imported as ROIs. The Golgi ROIs were used to measure mean
437 RUSH intensity in the Golgi at each time point. The mean RUSH intensities were subtracted by
438 background signals. Then, the maximum mean value of RUSH during the time course of the single-
439 cell images was used to divide the RUSH intensities, thus normalizing the maximal RUSH
440 intensities in the Golgi marker set to 1. The time course images for each single cell were analyzed
441 separately and combined to generate the mean RUSH intensity in each time point and its standard
442 deviation, as described in the Figures. Three independently cultured cells were analyzed, and their
443 images were combined to generate the final data.

444

445 **Secretion assay of LyzC-EGFP**

446 For the secretion assay, $5x10^5$ cells stably expressing LyzC-EGFP were plated in a 6 well
447 plate. After 24 hours cells were pretreated with 70μM 2-APB and DMSO. After that incubated in
448 grown medium containing 2-APB and DMSO for 1 hour. Cells and media were collected
449 separately. Cells were lysed using RIPA buffer. Collected grown media was incubated overnight
450 with GFP-trap beads at 4°C. On the next day the beads were washed 4 times with DPBS and then
451 protein was eluted from the beads by boiling it in 2X Laemmli SDS sample buffer (Biorad). Cell
452 lysates and IP fractions were analyzed by western blotting.

453 **Live cell imaging and FRET analysis**

454 For live cell imaging, DMEM without phenol red containing 4.5 mg ml – glucose, 25 mM
455 HEPES, 2 mM glutamine (Life Technologies) supplemented with 10 % FBS was used. Cells were
456 seeded on Glass bottom dishes (D35-14-1.5-N, Cellvis) on density $5x10^4$ per dish. Next day to
457 induce transgene expression doxycycline at final concentration 1ug/mL was added. After 24 hours
458 of doxycycline was cancelled and cells were incubated in imaging media for additional 24 hours.
459 ImageJ (National Institutes of Health) was used for basic image processing. All analyses were
460 done using custom-written software (MATLAB R2014a; MathWorks). To manipulate
461 intracellular Ca^{2+} levels as well as inducing Ca^{2+} flux following drugs at corresponding
462 concentrations were used: calcium ionomycin (I3909-1ML, Sigma) at 1μM; 2-APB (100065-
463 100MG, Millipore) at 70μM, Histamine (H7125-1G, Sigma) 1 μM solution, BAPTA-AM
464 (126150-97-8, Millipore) at 25 μM final concentration. To inhibit protein synthesis, cells were
465 treated with cycloheximide at concentration 10ug/mL (DSC81040-5, Dot Scientific Inc).

466 **FRET sensor calibration experiment.**

467 Free Ca^{2+} calibration solutions were made by using Calcium Calibration Buffer Kit #1
468 (Cat. No. C3008MP, Biotium) according to standard protocol. To perform FRET calibration

469 experiment HeLa cell line stably expressing CYTO-Twitch2b was used. $1x10^5$ cells were plated
470 into Glass bottom dishes (D35-14-1.5-N, Cellvis) and doxycycline was added to the media at final
471 concentration 1 ug/mL. After 24 hours for each plate growth media was washed twice with 10mM
472 EGTA, 100mM KCl, 10mM MOPS (pH7.2). To chelate residual Ca^{2+} cells were incubated in
473 10mM EGTA, 100mM KCl, 10mM MOPS (pH7.2) with 1 μM ionomycin for 20 min at RT. 2ml
474 of stock solutions with free Ca^{2+} concentrations ranging from 0 μM to 39 μ μM were added to
475 cells and FRET indexes were measured for each condition.

476 **FRET imaging and analysis**

477 These analyses were done essentially as previously described (Kumar et al., 2016). High
478 resolution live FRET imaging was performed on Nikon Eclipse Ti widefiled microscope equipped
479 with a cooled charged-coupled device Cool SNAP HQ2 camera, using a ×100, 1.49 NA oil
480 objective at 37 °C. Images were acquired using Micromanager software. Three sequential images
481 with 500 ms exposure time were acquired with the following filter combinations: donor (Teal)
482 channel with 460/20 (excitation filter-ex), T455lp (dichroic mirror-di) and 500/22 (emission filter-
483 em); FRET channel with 460/20 (ex), T455lp (di) and 535/30 (em); and acceptor (Venus) channel
484 with 492/18 (ex), T515lp (di) and 535/30 (em) filter combinations. All filters and dichroic were
485 purchased from Chroma Technology. For data analysis, donor leakage was determined from HeLa
486 cells transiently transfected with Vinculin-Teal, whereas acceptor cross excitation was obtained
487 from Vinculin-Venus transfected cells. For all the calculations, respective background subtraction,
488 illumination gradient, and pixel shift correction were performed followed by three-point
489 smoothening. The slope of pixel-wise donor or acceptor channel intensity versus FRET channel
490 intensity gives leakage (x) or cross-excitation (y) fraction, respectively. FRET map and pixel-wise

491 FRET index for the sensors were determined from FRETindex =
492 [FRETchannel−x(Donorchannel)− y(Acceptorchannel)]/[Acceptorchannel]
493 ImageJ (National Institutes of Health) was used for basic image thresholding. Mean FRET
494 index per cell was calculated for each region within the mask. Student's t test was performed
495 between the two groups to calculate statistical significance and p-value. At least $P < 0.05$ was
496 considered significant. All analyses were done using custom-written software (MATLABR2020b;
497 MathWorks) (Kumar et al., 2016).

498 **siRNA delivery and western blotting**

499 Knockdown of VAPA and VAPB proteins was performed by using siRNA (VAPA: 5'-
500 AACTAATGGAAGAGTGTAAAA-3'; VAPB: 5'-AAGAAGGTTATGGAAGAATGT-
501 3')(Wakana et al., 2021). Non-targeting siRNA was purchased from Qiagen (Catalog No. –
502 1027281) and used as reference negative control. Knockdown of VAPA and VAPB proteins was
503 achieved by combined transfection (siVAPA and siVAPB) by using LipofectRNAiMAX
504 according to standard protocol. Knockdown efficiency was confirmed by Western blotting of cell
505 lysates in radioimmunoprecipitation assay (RIPA) buffer (50 mM Tris-HCl, pH 7.4 [American
506 Bioanalytical], 150 mM NaCl [American Bioanalytical], 1% Triton X100 [American
507 Bioanalytical], 1% sodium deoxycholate [Sigma-Aldrich], and 0.1% SDS [American
508 Bioanalytical] in milliQ water); protease and phosphatase inhibitor (Thermo Fisher Scientific) was
509 added just before extraction. Cell lysate was resolved using SDS-PAGE and transferred to the
510 nitrocellulose membrane (Biorad Laboratories) using a transfer system (Trans-Blot Turbo; Bio-
511 Rad Laboratories). The membrane was blocked using 5% skimmed milk (American Bioanalytical)
512 in TBS with 0.1% Tween 20 (TBST) for 1 hour and incubated with the following primary
513 antibodies diluted in 5% milk with TBST overnight at 4°C: Anti-β-actin (1:5000, A5441-.2ML

514 Sigma); Anti-VAPA (1:1000, SAB1402460-100G, Sigma); Anti-hVAPB (1:2000, MAB58551
515 R&D systems); anti-GFP (1:1000, 11814460001, Roche). Membrane was washed 3 times with 5%
516 milk TBST and incubated with HRP-conjugated secondary antibodies (1:5000, 32230/32260;
517 Invitrogen). Data was visualized using chemiluminescence detection on ChemiDoc Touch (Bio-
518 Rad Laboratories)**.**

519 **Graphical data and image design**

520 Graphs were plotted in GraphPad Prism version 9.2.0 for Mac, GraphPad Software, San Diego,
521 California USA. Images were compiled using Adobe Illustrator 2022 (Adobe Inc. (2022). Adobe
522 Illustrator. Retrieved from https://adobe.com/products/illustrator). Schemes were designed using
523 Biorender software (biorender.com).

524

525

Acknowledgments

We thank Dr. Pietro de Camilli for providing VAPA/VAPB-dKO cell lines and the Burd lab for discussions and support. Julia von Blume is funded by a Yale-start up grant and by the National Institute of General Medical Sciences of the NIH under the award number GM134083-01, an Administrative Supplement 3R01GM134083-03S1 and a Project and Feasibility award from Yale Diabetic Research Center (GR112420).

Author Contributions

B.R.Ramazanov and J.von Blume designed the experiments. B.R.Ramazanov carried out the experiments and analyzed the data. A.Kumar and M.Schwartz provided support in FRET data analysis and composed the software code for data analysis. A. Parchure and Y.Kim performed and analyzed secretion assays. O.Griesbeck provided Twitch sensors encoding plasmids. M.Schwartz provided the equipment. B.R.Ramazanov and J.von Blume wrote the paper.

Declaration of Interest

The authors declare no competing financial interests.

545 **Abbreviations**

546 ER - Endoplasmic reticulum

547 FRET - Fluorescence resonance energy transfer

548 nm - nanometer

549 TGN - Trans Golgi Network

550

551 # References

552 Barlowe, C.K., and E.A. Miller. 2013. Secretory protein biogenesis and traffic in the early
553 secretory pathway. *Genetics*. 193:383-410.
554 Berridge, M.J., M.D. Bootman, and H.L. Roderick. 2003. Calcium signalling: dynamics,
555 homeostasis and remodelling. *Nat Rev Mol Cell Biol*. 4:517-529.
556 Boncompain, G., S. Divoux, N. Gareil, H. de Forges, A. Lescure, L. Latreche, V. Mercanti, F.
557 Jollivet, G. Raposo, and F. Perez. 2012. Synchronization of secretory protein traffic in
558 populations of cells. *Nat Methods*. 9:493-U120.
559 Carafoli, E. 2002. Calcium signaling: A tale for all seasons. *Proceedings of the National Academy*
560 *of Sciences*. 99:1115-1122.
561 Crevenna, A.H., B. Blank, A. Maiser, D. Emin, J. Prescher, G. Beck, C. Kienzle, K. Bartnik, B.
562 Habermann, M. Pakdel, H. Leonhardt, D.C. Lamb, and J. von Blume. 2016. Secretory
563 cargo sorting by Ca2+-dependent Cab45 oligomerization at the trans-Golgi network. *J*
564 *Cell Biol*. 213:305-314.
565 De Matteis, M.A., and A. Luini. 2008. Exiting the Golgi complex. *Nat Rev Mol Cell Biol*. 9:273-
566 284.
567 Deng, Y., M. Pakdel, B. Blank, E.L. Sundberg, C.G. Burd, and J. von Blume. 2018. Activity of the
568 SPCA1 Calcium Pump Couples Sphingomyelin Synthesis to Sorting of Secretory Proteins
569 in the Trans-Golgi Network. *Dev Cell*. 47:464-478 e468.
570 Deng, Y., F.E. Rivera-Molina, D.K. Toomre, and C.G. Burd. 2016. Sphingomyelin is sorted at the
571 trans Golgi network into a distinct class of secretory vesicle. *Proc Natl Acad Sci U S A*.
572 113:6677-6682.
573 Di Martino, R., L. Sticco, and A. Luini. 2019. Regulation of cargo export and sorting at the trans-
574 Golgi network. *FEBS Lett*. 593:2306-2318.
575 Dickenson, J.M., and S.J. Hill. 1994. Selective potentiation of histamine H1-receptor stimulated
576 calcium responses by 1,4-dithiothreitol in DDT1MF-2 cells. *Biochem Pharmacol*.
577 48:1721-1728.
578 Dong, R., Y. Saheki, S. Swarup, L. Lucast, J.W. Harper, and P. De Camilli. 2016. Endosome-ER
579 Contacts Control Actin Nucleation and Retromer Function through VAP-Dependent
580 Regulation of PI4P. *Cell*. 166:408-423.
581 Dunlop, M.H., A.M. Ernst, L.K. Schroeder, D.K. Toomre, G. Lavieu, and J.E. Rothman. 2017. Land-
582 locked mammalian Golgi reveals cargo transport between stable cisternae. *Nat*
583 *Commun*. 8.
584 Dunphy, W.G., and J.E. Rothman. 1985. Compartmental organization of the Golgi stack. *Cell*.
585 42:13-21.
586 Ford, C., A. Parchure, J. von Blume, and C.G. Burd. 2021. Cargo sorting at the trans-Golgi
587 network at a glance. *J Cell Sci*. 134.
588 Gillon, A.D., C.F. Latham, and E.A. Miller. 2012. Vesicle-mediated ER export of proteins and
589 lipids. *Biochim Biophys Acta*. 1821:1040-1049.
590 Glick, B.S., T. Elston, and G. Oster. 1997. A cisternal maturation mechanism can explain the
591 asymmetry of the Golgi stack. *FEBS Lett*. 414:177-181.
592 Glick, B.S., and A. Luini. 2011. Models for Golgi traffic: a critical assessment. *Cold Spring Harb*
593 *Perspect Biol*. 3:a005215.

594 Glick, B.S., and A. Nakano. 2009. Membrane Traffic Within the Golgi Apparatus. *Annual Review*
595 *of Cell and Developmental Biology*. 25:113-132.
596 Grashoff, C., B.D. Hoffman, M.D. Brenner, R. Zhou, M. Parsons, M.T. Yang, M.A. McLean, S.G.
597 Sligar, C.S. Chen, T. Ha, and M.A. Schwartz. 2010. Measuring mechanical tension across
598 vinculin reveals regulation of focal adhesion dynamics. *Nature*. 466:263-266.
599 Guo, Y.S., D.W. Sirkis, and R. Schekman. 2014. Protein Sorting at the trans-Golgi Network. *Annu*
600 *Rev Cell Dev Bi*. 30:169-206.
601 Kawano, M., K. Kumagai, M. Nishijima, and K. Hanada. 2006. Efficient trafficking of ceramide
602 from the endoplasmic reticulum to the Golgi apparatus requires a VAMP-associated
603 protein-interacting FFAT motif of CERT. *J Biol Chem*. 281:30279-30288.
604 Kelly, R.B. 1985. Pathways of Protein Secretion in Eukaryotes. *Science*. 230:25-32.
605 Kienzle, C., N. Basnet, A.H. Crevenna, G. Beck, B. Habermann, N. Mizuno, and J. von Blume.
606 2014. Cofilin recruits F-actin to SPCA1 and promotes Ca2+-mediated secretory cargo
607 sorting. *J Cell Biol*. 206:635-654.
608 Kienzle, C., and J. von Blume. 2014. Secretory cargo sorting at the trans-Golgi network. *Trends*
609 *Cell Biol*. 24:584-593.
610 Kumagai, K., and K. Hanada. 2019. Structure, functions and regulation of CERT, a lipid-transfer
611 protein for the delivery of ceramide at the ER-Golgi membrane contact sites. *Febs*
612 *Letters*. 593:2366-2377.
613 Kumar, A., M. Ouyang, K. Van den Dries, E.J. McGhee, K. Tanaka, M.D. Anderson, A. Groisman,
614 B.T. Goult, K.I. Anderson, and M.A. Schwartz. 2016. Talin tension sensor reveals novel
615 features of focal adhesion force transmission and mechanosensitivity. *J Cell Biol*.
616 213:371-383.
617 Ladinsky, M.S., C.C. Wu, S. McIntosh, J.R. McIntosh, and K.E. Howell. 2002. Structure of the
618 Golgi and distribution of reporter molecules at 20 degrees C reveals the complexity of
619 the exit compartments. *Mol Biol Cell*. 13:2810-2825.
620 Lebreton, S., S. Paladino, D. Liu, M. Nitti, J. von Blume, P. Pinton, and C. Zurzolo. 2021. Calcium
621 levels in the Golgi complex regulate clustering and apical sorting of GPI-APs in polarized
622 epithelial cells. *Proc Natl Acad Sci U S A*. 118.
623 Lehto, M., and V.M. Olkkonen. 2003. The OSBP-related proteins: a novel protein family involved
624 in vesicle transport, cellular lipid metabolism, and cell signalling. *Biochim Biophys Acta*.
625 1631:1-11.
626 Lev, S. 2010. Non-vesicular lipid transport by lipid-transfer proteins and beyond. *Nat Rev Mol*
627 *Cell Biol*. 11:739-750.
628 Li, Z.J., I.P. Michael, D.X. Zhou, A. Nagy, and J.M. Rini. 2013. Simple piggyBac transposon-based
629 mammalian cell expression system for inducible protein production. *P Natl Acad Sci*
630 *USA*. 110:5004-5009.
631 Lissandron, V., P. Podini, P. Pizzo, and T. Pozzan. 2010. Unique characteristics of Ca2+
632 homeostasis of the trans-Golgi compartment. *Proc Natl Acad Sci U S A*. 107:9198-9203.
633 Lujan, P., and F. Campelo. 2021. Should I stay or should I go? Golgi membrane spatial
634 organization for protein sorting and retention. *Arch Biochem Biophys*. 707.
635 Maruyama, T., T. Kanaji, S. Nakade, T. Kanno, and K. Mikoshiba. 1997. 2APB, 2-
636 aminoethoxydiphenyl borate, a membrane-penetrable modulator of Ins(1,4,5)P3-
637 induced Ca2+ release. *J Biochem*. 122:498-505.

638 Masone, M.C., V. Morra, and R. Venditti. 2019. Illuminating the membrane contact sites
639 between the endoplasmic reticulum and the trans-Golgi network. *FEBS Lett*. 593:3135-
640 3148.
641 Matlin, K.S., and K. Simons. 1983. Reduced temperature prevents transfer of a membrane
642 glycoprotein to the cell surface but does not prevent terminal glycosylation. *Cell*.
643 34:233-243.
644 Mesmin, B., J. Bigay, J. Polidori, D. Jamecna, S. Lacas-Gervais, and B. Antonny. 2017. Sterol
645 transfer, PI4P consumption, and control of membrane lipid order by endogenous OSBP.
646 *Embo J*. 36:3156-3174.
647 Mesmin, B., J. Bigay, J.M. von Filseck, S. Lacas-Gervais, G. Drin, and B. Antonny. 2013. A Four-
648 Step Cycle Driven by PI(4)P Hydrolysis Directs Sterol/PI(4)P Exchange by the ER-Golgi
649 Tether OSBP. *Cell*. 155:830-843.
650 Missiaen, L., L. Dode, J. Vanoevelen, L. Raeymaekers, and F. Wuytack. 2007. Calcium in the Golgi
651 apparatus. *Cell Calcium*. 41:405-416.
652 Mostov, K.E., and M.H. Cardone. 1995. Regulation of protein traffic in polarized epithelial cells.
653 *Bioessays*. 17:129-138.
654 Nakano, A., and A. Luini. 2010. Passage through the Golgi. *Curr Opin Cell Biol*. 22:471-478.
655 Pakdel, M., and J. von Blume. 2018. Exploring new routes for secretory protein export from the
656 trans-Golgi network. *Mol Biol Cell*. 29:235-240.
657 Pfeffer, S.R., and J.E. Rothman. 1987. Biosynthetic protein transport and sorting by the
658 endoplasmic reticulum and Golgi. *Annu Rev Biochem*. 56:829-852.
659 Phillips, M.J., and G.K. Voeltz. 2016. Structure and function of ER membrane contact sites with
660 other organelles. *Nat Rev Mol Cell Biol*. 17:69-82.
661 Pizzo, P., V. Lissandron, P. Capitanio, and T. Pozzan. 2011. Ca2+ signalling in the Golgi
662 apparatus. *Cell Calcium*. 50:184-192.
663 Pizzo, P., V. Lissandron, and T. Pozzan. 2010. The trans-golgi compartment: A new distinct
664 intracellular Ca store. *Commun Integr Biol*. 3:462-464.
665 Ramazanov, B.R., M.L. Tran, and J. von Blume. 2021. Sending out molecules from the TGN. *Curr*
666 *Opin Cell Biol*. 71:55-62.
667 Rizzuto, R., M. Brini, M. Murgia, and T. Pozzan. 1993. Microdomains with High Ca2+ Close to
668 Ip(3)-Sensitive Channels That Are Sensed by Neighboring Mitochondria. *Science*.
669 262:744-747.
670 Rizzuto, R., P. Pinton, W. Carrington, F.S. Fay, K.E. Fogarty, L.M. Lifshitz, R.A. Tuft, and T. Pozzan.
671 1998. Close contacts with the endoplasmic reticulum as determinants of mitochondrial
672 Ca2+ responses. *Science*. 280:1763-1766.
673 Scherer, P.E., G.Z. Lederkremer, S. Williams, M. Fogliano, G. Baldini, and H.F. Lodish. 1996.
674 Cab45, a novel (Ca2+)-binding protein localized to the Golgi lumen. *J Cell Biol*. 133:257-
675 268.
676 Sepulveda, M.R., D. Marcos, M. Berrocal, L. Raeymaekers, A.M. Mata, and F. Wuytack. 2008.
677 Activity and localization of the secretory pathway Ca2+-ATPase isoform 1 (SPCA1) in
678 different areas of the mouse brain during postnatal development. *Mol Cell Neurosci*.
679 38:461-473.
680 Stalder, D., and D.C. Gershlick. 2020. Direct trafficking pathways from the Golgi apparatus to
681 the plasma membrane. *Semin Cell Dev Biol*. 107:112-125.

682 Tang, B.L. 2001. Protein trafficking mechanisms associated with neurite outgrowth and
683 polarized sorting in neurons. *J Neurochem*. 79:923-930.
684 Thillaiappan, N.B., A.P. Chavda, S.C. Tovey, D.L. Prole, and C.W. Taylor. 2017. Ca(2+) signals
685 initiate at immobile IP3 receptors adjacent to ER-plasma membrane junctions. *Nat*
686 *Commun*. 8:1505.
687 Uhlen, M., L. Fagerberg, B.M. Hallstrom, C. Lindskog, P. Oksvold, A. Mardinoglu, A. Sivertsson, C.
688 Kampf, E. Sjostedt, A. Asplund, I. Olsson, K. Edlund, E. Lundberg, S. Navani, C.A.
689 Szigyarto, J. Odeberg, D. Djureinovic, J.O. Takanen, S. Hober, T. Alm, P.H. Edqvist, H.
690 Berling, H. Tegel, J. Mulder, J. Rockberg, P. Nilsson, J.M. Schwenk, M. Hamsten, K. von
691 Feilitzen, M. Forsberg, L. Persson, F. Johansson, M. Zwahlen, G. von Heijne, J. Nielsen,
692 and F. Ponten. 2015. Proteomics. Tissue-based map of the human proteome. *Science*.
693 347:1260419.
694 Venditti, R., M.C. Masone, and M.A. De Matteis. 2020. ER-Golgi membrane contact sites.
695 *Biochem Soc Trans*. 48:187-197.
696 Venditti, R., M.C. Masone, L.R. Rega, G. Di Tullio, M. Santoro, E. Polishchuk, I.C. Serrano, V.M.
697 Olkkonen, A. Harada, D.L. Medina, R. La Montagna, and M.A. De Matteis. 2019. The
698 activity of Sac1 across ER-TGN contact sites requires the four-phosphate-adaptor-
699 protein-1. *J Cell Biol*. 218:783-797.
700 von Blume, J., A.M. Alleaume, G. Cantero-Recasens, A. Curwin, A. Carreras-Sureda, T.
701 Zimmermann, J. van Galen, Y. Wakana, M.A. Valverde, and V. Malhotra. 2011.
702 ADF/cofilin regulates secretory cargo sorting at the TGN via the Ca2+ ATPase SPCA1. *Dev*
703 *Cell*. 20:652-662.
704 von Blume, J., A.M. Alleaume, C. Kienzle, A. Carreras-Sureda, M. Valverde, and V. Malhotra.
705 2012. Cab45 is required for Ca(2+)-dependent secretory cargo sorting at the trans-Golgi
706 network. *J Cell Biol*. 199:1057-1066.
707 Wakana, Y., K. Hayashi, T. Nemoto, C. Watanabe, M. Taoka, J. Angulo-Capel, M.F. Garcia-Parajo,
708 H. Kumata, T. Umemura, H. Inoue, K. Arasaki, F. Campelo, and M. Tagaya. 2021. The ER
709 cholesterol sensor SCAP promotes CARTS biogenesis at ER-Golgi membrane contact
710 sites. *J Cell Biol*. 220.
711 Wong, A.K.C., P. Capitanio, V. Lissandron, M. Bortolozzi, T. Pozzan, and P. Pizzo. 2013.
712 Heterogeneity of Ca-2 handling among and within Golgi compartments. *J Mol Cell Biol*.
713 5:266-276.
714 Zanetti, G., S. Prinz, S. Daum, A. Meister, R. Schekman, K. Bacia, and J.A. Briggs. 2013. The
715 structure of the COPII transport-vesicle coat assembled on membranes. *Elife*. 2:e00951.
716

Main Figures

Main Figure legends

Figure 1. Inhibition of IP3R activity delays TGN export of Cab45 clients
(A) Schematic representation of the Retention Using Streptavidin Hooks (RUSH) assay with fluorescent tagged client molecules. (B) Representative immunofluorescence images of the RUSH experiments showing COMP-EGFP transport in HeLa lines treated with DMSO and 70 nM 2-APB. HeLa cells were transfected with KDEL-IRES-SBP-COMP-EGFP and fixed at 0, 20, 40, and 60 min after the addition of biotin. Z-stack images (d = 0.2 µm) were analyzed. The arrowheads indicate cytoplasmic vesicles. Scale bars, 10 µm. (C) The numbers of COMP budding vesicles from RUSH experiments with KDEL-IRES-SBP-COMP-EGFP in HeLa lines treated with DMSO and 2-APB were quantified. The cytoplasmic vesicles were counted at each time point by analyzing z-stack images (d = 0.2 µm). Scatter dot plot represents the means ± SD of at least three independent experiments (n > 30 cells per condition). Statistical test, Kruskal–Wallis. (D) Plot representing normalized average fluorescence intensity of COMP-EGFP in cells by FACS at 0, 60 and 120 minutes of RUSH experiments. (E) Plot representing normalized fluorescence intensity of LyzC-EGFP within TGN (ROI was defined by GALNT1 area) in cells treated with DMSO and 2-APB. (F) Western blot showing LyzC-GFP in Hela cells treated with DMSO and 2-APB in cell lysates and in secreted medium (top) and β-actin as a loading control.

Figure 2. Depletion of VAPA and VAPB delays TGN export of Cab45 clients
(A) Representative immunofluorescence images of RUSH experiments showing COMP-GFP transport in HeLa lines treated with siRNA against VAPA and VAPB proteins. Cells were transfected with KDEL-IRES-SBP-COMP-EGFP and fixed at 0, 20, 40, and 60 min after the addition of biotin. Z-stack images (d = 0.2 µm) were analyzed. Scale bars, 10 µm. (B) The numbers of COMP budding vesicles were quantified. The cytoplasmic vesicles were counted at each time point by analyzing z-stack images (d = 0.2 µm). Scatter dot plot represents the means ± SD of at least three independent experiments (n > 30 cells per condition). Statistical test, Kruskal–Wallis. (C) Plot representing normalized average fluorescence intensity of COMP-EGFP in cells by FACS at 0, 60 and 120 minutes of RUSH experiments in HeLa WT and VAPA/VAPB-dKO lines (D) Plot representing normalized fluorescence intensity of LyzC-EGFP within TGN (ROI was defined by Galnt1 area) in cells treated with non-targeting (control) siRNA and siRNA targeting VAPA and VAPB. (E) Expression of VAPA and VAPB proteins in Hela WT line transfected with control (non-targeting) siRNA, Hela line transfected with siVAPA/siVAPB and Hela VAPA/VAPB-dKO line. β-actin was used as a loading control.

Figure 3. MCS targeting FRET sensor responses to changes of Ca^{2+} concentration at ER-TGN MCS.
(A) Schematic representation of OSBP and Twitch2b Calcium Sensor targeting Endoplasmic Reticulum-Golgi membrane contact sites. PH domain of OSBP binds to PI4P on the outer leaflet of the TGN membrane and FFAT domain interacts with VAPA on the ER membrane. (B) Calibration curve for Twitch2b sensor performed used buffer with increasing concentration of free Ca^{2+} ions demonstrating correlation between FRET indices and free Ca^{2+}. (See Materials and Methods for a detailed description). (C) Pseudocolor map of FRET index and dot plot (D) representing FRET indices for PH-FFAT-Twitch2b and PH-FFAT-Twitch9x within Golgi ROI of

live cells and at steady state (***p<0.05). (E) Pseudocolor map of FRET index and dot plot (F) representing FRET indices for PH-FFAT-Twitch2b at steady state and treated with 25uM BAPTA-AM for 20 min (***p<0.05). (G) Pseudocolor map of FRET index and dot plot (H) representing FRET indices for PH-FFAT-Twitch2b at steady state and treated with 1uM ionomycin for 20 min (***p<0.05). (I) Pseudocolor map of FRET index and dot plot (J) representing FRET indices for PH-FFAT-Twitch2b at steady state and treated with 1uM Histamine for 2 min (***p<0.05). Pseudocolor bar FRET index value in range 0-0.4.

Figure 4. Ca^{2+} flux at ER-TGN MCS is coupled to protein trafficking

(A) Schematic representation of experiment and effect on protein trafficking in live cells during 20°C block and cycloheximide (CHX) treatment. (B) Pseudocolor maps of FRET index for PH-FFAT-Twitch2b within Golgi ROI of live cells at described above conditions. Pseudocolor bar FRET index value in range 0-0.4. (C) Dot plot representing FRET index for PH-FFAT-Twitch2b at steady state, after 20°C block for 1 and 2 hours and after 10 min recovery at 37°C (***p<0.05). (D) Dot plot representing FRET index for PH-FFAT-Twitch2b at steady state, treated with CHX for 1, 2, 4 hours and after 1h 20°C block. (***p<0.05), (E) Dot plot representing normalized FRET index for PH-FFAT-Twitch2b at steady state, after 1h 20°C block and effect of ionomycin at 37°C and 20°C conditions (***p<0.05).

Figure 5A. The model depicting the role of contact sites and IP3R-dependent release of Calcium ions for SPCA1 dependent sorting at TGN.

Supplementary data

Supplementary Figure legends

Supplementary 1. RUSH experiments using Cab45 clients demonstrate that delay in protein trafficking takes place at TGN

(A) Representative histograms plotting fluorescence intensity distribution of COMP-GFP in cells at 30, 60 and 120 minutes (shown in red) during RUSH experiment compared to timepoint "0" (shown in green overlay) in HeLa WT cells line treated with DMSO (upper row), HeLa WT cells treated with 2-APB (middle row), and HeLa VAPA/VAPB-dKO line (bottom row). 10.000 cells analyzed for each condition. (B) Graph depicting mean normalized fluorescence intensity (F.I.) of RUSH LyzC-EGFP in BFP-GALNT1 (Golgi marker) region of interest (ROI) from and after the time when the maximal LyzC-EGFP F.I. is reached in the ROI (peak Golgi F.I.). The decrease in LyzC-EGFP F.I. represents the Golgi exit in HeLa line treated with DMSO (black) versus 2-APB treated (red). At least 10 cells from independent experiments for each condition were analyzed with nonlinear regression (exponential function) indicated in the plot using GraphPad Prism9 built-in regression. (C) Graph depicting mean normalized fluorescence intensity (F.I.) of RUSH LyzC-EGFP in BFP-GALNT1 (Golgi marker) region of interest (ROI) from and after the time when the maximal LyzC-EGFP F.I. is reached in the ROI (peak Golgi F.I.). The decrease in LyzC-EGFP F.I. represents the Golgi exit in HeLa line transfected with control siRNA (black) versus Hela line transfected with siRNA to VAPA and VAPB (red). At least 10 cells from independent experiments for each condition were analyzed with nonlinear regression (exponential function) indicated in the plot using GraphPad Prism9 built-in regression.

Supplementary 2. VAPA/VAPB dKO HeLa lines demonstrate delay in TGN export of Cab45 clients in RUSH experiments

(A) Representative immunofluorescence images of RUSH experiments showing LyzC-GFP transport in HeLa WT and VAPA/B-dKO cell lines. Cells were transfected with KDEL-IRES-SBP-LyzC-EGFP and fixed at 0, 20, 40, and 60 min after the addition of biotin. Z-stack images (d = 0.2 µm) were analyzed. The arrowheads indicate cytoplasmic vesicles. Scale bars, 10 µm. (B) Representative immunofluorescence images of RUSH experiments showing COMP-GFP transport in HeLa WT and VAPA/B-dKO cell lines. Cells were transfected with KDEL-IRES-SBP-COMP-EGFP and fixed at 0, 20, 40, and 60 min after the addition of biotin. Z-stack images (d = 0.2 µm) were analyzed. The arrowheads indicate cytoplasmic vesicles. Scale bars, 10 µm. (C) The numbers of LyzC budding vesicles were quantified. The cytoplasmic vesicles were counted at each time point by analyzing z-stack images (d = 0.2 µm). Scatter dot plot represents the means ± SD of at least three independent experiments (n > 30 cells per condition). Statistical test, Kruskal–Wallis. (D) The numbers of COMP budding vesicles were quantified. The cytoplasmic vesicles were counted at each time point by analyzing z-stack images (d = 0.2 µm). Scatter dot plot represents the means ± SD of at least three independent experiments (n > 30 cells per condition). Statistical test, Kruskal–Wallis.

Supplementary 3. MCS targeting FRET sensors localize with TGN markers.

(A) Schematic representation of the domain structure of OSBP (top construct) and Twitch sensors fused proteins targeting ER-Golgi contact sites (N-PH-FFAT-Twitch and PH-FFAT-Twitch) as well as sensors targeting ER (fused with VAPA protein) and cytoplasmic version (two bottom constructs) used in this study. (B) IF images of HeLa lines stably expressing Twitch2b sensor targeting cytoplasm, ER and ER-TGN contact sites. (C) IF images of HeLa line expressing Twitch2b sensor targeting ER-TGN contact sites and its localization compared to TGN46 (TGN marker). (D) IF images of HeLa line expressing Twitch2b sensor targeting ER-TGN contact sites and its localization compared to GM130 (cis Golgi marker). (E) Dot plot representing FRET index for PH-FFAT-Twitch2b and PH-FFAT-Twitch7x, PH-FFAT-Twitch8x and PH-FFAT-Twitch9x within Golgi ROI of live cells and at steady state (***$p<0.05$); (F) Dot plot representing FRET index for PH-FFAT-Twitch2b and N-PH-FFAT-Twotch2b in cells at steady state. (G) Dot plot representing FRET index for N-PH-FFAT-Twitch2b cells at steady state and treated with 1uM ionomycin for 20 min (***$p<0.05$). (H) Dot plot representing FRET index for N-PH-FFAT-Twitch2b cells at steady state and treated with 1uM Histamine for 2 min(***$p<0.05$).

Supplementary 4. Calibration procedures of Twitch2b sensor and fluorescence channels for FRET experiments

(A) Schematic representation of the calibration experiment of Twich2b calcium sensor using Ca-EGTA buffers in live cells (Please see Materials and Methods section for detailed description). (B) Pseudocolor heatmap of FRET index for CYTO-Twitch2b during calibration experiment. Pseudocolor bar FRET index value in range 0-0.4. (C) Calibration of fluorescence channels for Twitch sensor using HeLa lines expressing PH-FFAT-mCerulean3 (only FRET donor), HeLa lines expressing PH-FFAT-cpVenus (only FRET acceptor)) and PH-FFAT-Twitch2b (FRET pair with calcium binding domain) sensor.

854 **Table legends**

855

856 Supplementary Table1. Twitch sensors and their affinity to Ca^{2+} ions.

857

FRET Sensor	**Calcium affinity of TnC (KD)**
Twitch 2b	200 nM
Twitch 7x	51.5 uM
Twitch 8x	139 uM
Twitch 9x	174 uM

858

859

860 Supplementary Table2. Twitch sensors and aminoacidic sequences of calcium binding domains.

861

FRET Sensor	**Amino acid sequence of Calcium binding domain of Twitch sensors**
Twitch 2b	MQVADASEEELSECFRIFDFDGN_GFIDREEFGDIIRLTGE QLTDEDVDEIFGDSDTDKN_GRIDFDEFLKMVENVQPIYP
Twitch 7x	MQVADASEEELSECFRIFDFDGNDGFIDREEFGDIIRLTGE QLTDEDVDEIFGDSDTDKN_GRIDFDEFLKMVENVQPIYP
Twitch 8x	MQVADASEEELSECFRIFDFDGN_GFIDREEFGDIIRLTGE QLTDEDVDEIFGDSDTDKNSGRIDFDEFLKMVENVQPIYP
Twitch 9x	MQ__DASEEELSECFRIFDKDGNDGFIDREEFGDIIRLTGE QLTDEDVDEIFGDSDTDKN_GRIDFDEFLKMVENVQPIYP

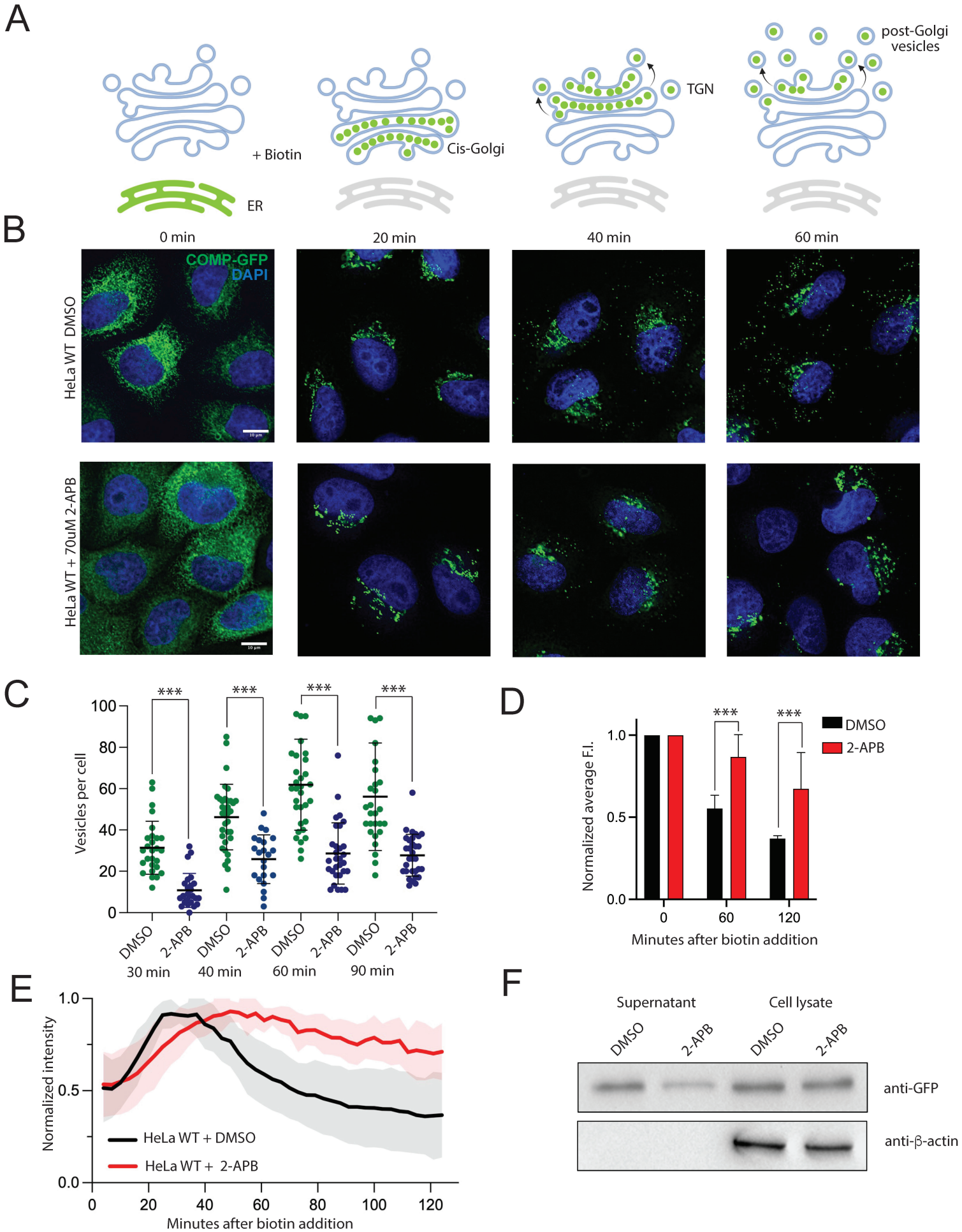

Figure 1. Inhibition of IP3R activity delays TGN export of Cab45 clients
(A) Schematic representation of the Retention Using Streptavidin Hooks (RUSH) assay with fluorescent tagged client molecules. (B) Representative immunofluorescence images of the RUSH experiments showing COMP-EGFP transport in HeLa lines treated with DMSO and 70 nM 2-APB. HeLa cells were transfected with KDEL-IRES-SBP-COMP-EGFP and fixed at 0, 20, 40, and 60 min after the addition of biotin. Z-stack images (d = 0.2 μm) were analyzed. The arrowheads indicate cytoplasmic vesicles. Scale bars, 10 μm. (C) The numbers of COMP budding vesicles from RUSH experiments with KDEL-IRES-SBP-COMP-EGFP in HeLa lines treated with DMSO and 2-APB were quantified. The cytoplasmic vesicles were counted at each time point by analyzing z-stack images (d = 0.2 μm). Scatter dot plot represents the means ± SD of at least three independent experiments (n > 30 cells per condition). Statistical test, Kruskal–Wallis. (D) Plot representing normalized average fluorescence intensity (F.I.) of COMP-EGFP in cells by FACS at 0, 60 and 120 minutes of RUSH experiments, ***p<0.001 (E) Plot representing normalized fluorescence intensity of LyzC-EGFP within TGN (ROI was defined by GALNT1 area) in cells treated with DMSO and 2-APB. (F) Western blot showing LyzC-GFP in Hela cells treated with DMSO and 2-APB in cell lysates and in secreted medium (top) and β-actin as a loading control.

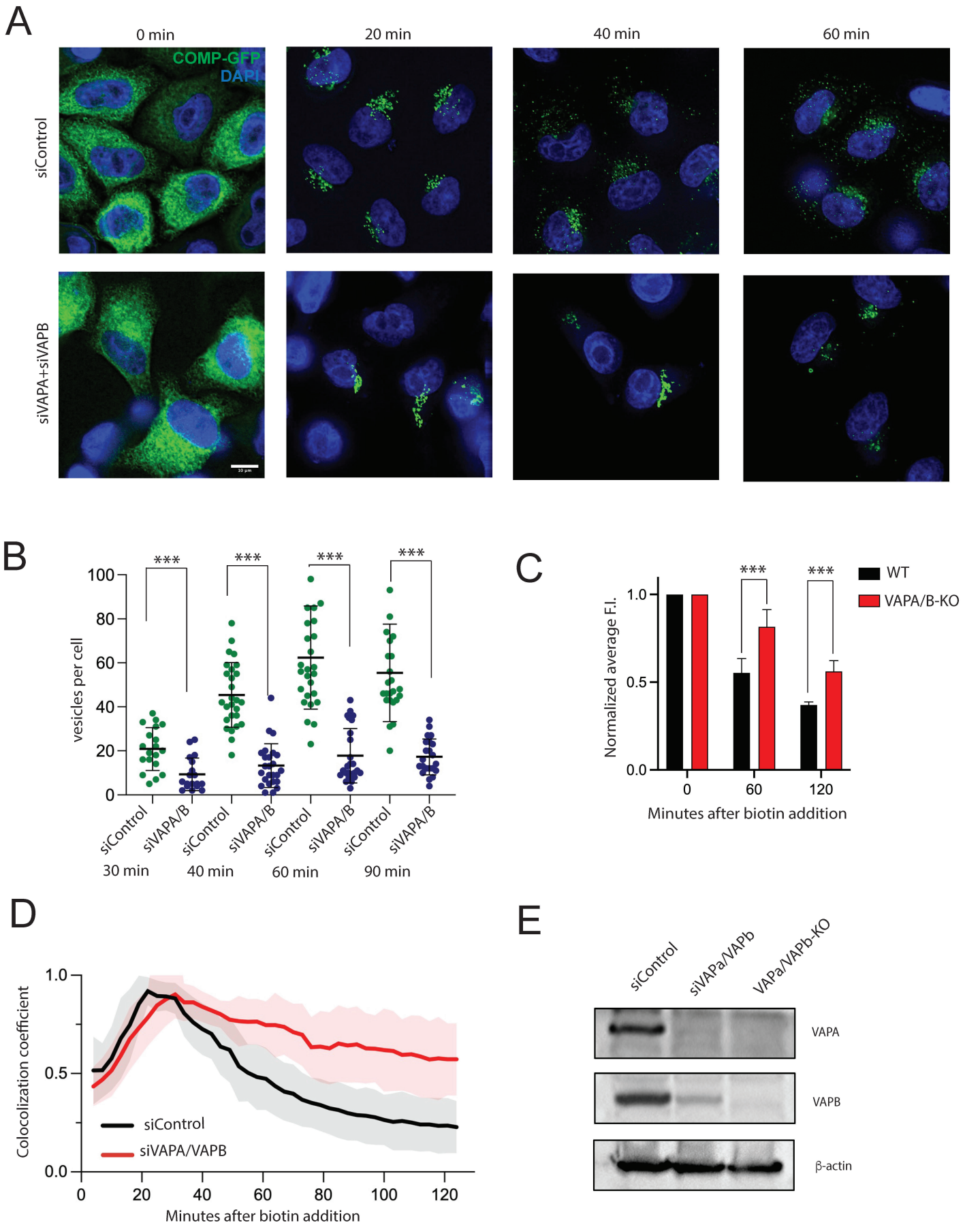

Figure 2. Depletion of VAPA and VAPB delays TGN export of Cab45 clients
(A) Representative immunofluorescence images of RUSH experiments showing COMP-GFP transport in HeLa lines treated with siRNA against VAPA and VAPB proteins. Cells were transfected with KDEL-IRES-SBP-COMP-EGFP and fixed at 0, 20, 40, and 60 min after the addition of biotin. Z-stack images (d = 0.2 μm) were analyzed. Scale bars, 10 μm. (B) The numbers of COMP budding vesicles were quantified. The cytoplasmic vesicles were counted at each time point by analyzing z-stack images (d = 0.2 μm). Scatter dot plot represents the means ± SD of at least three independent experiments (n > 30 cells per condition). Statistical test, Kruskal–Wallis. (C) Plot representing normalized average fluorescence intensity (F.I.) of COMP-EGFP in cells by FACS at 0, 60 and 120 minutes of RUSH experiments in HeLa WT and VAPA/VAPB-dKO lines, ***p<0.001; (D) Plot representing normalized fluorescence intensity of LyzC-EGFP within TGN (ROI was defined by GalNt1 area) in cells treated with non-targeting (control) siRNA and siRNA targeting VAPA and VAPB. (E) Expression of VAPA and VAPB proteins in Hela WT line transfected with control (non-targeting) siRNA, Hela line transfected with siVAPA/siVAPB and Hela VAPA/VAPB-dKO line. β-actin was used as a loading control.

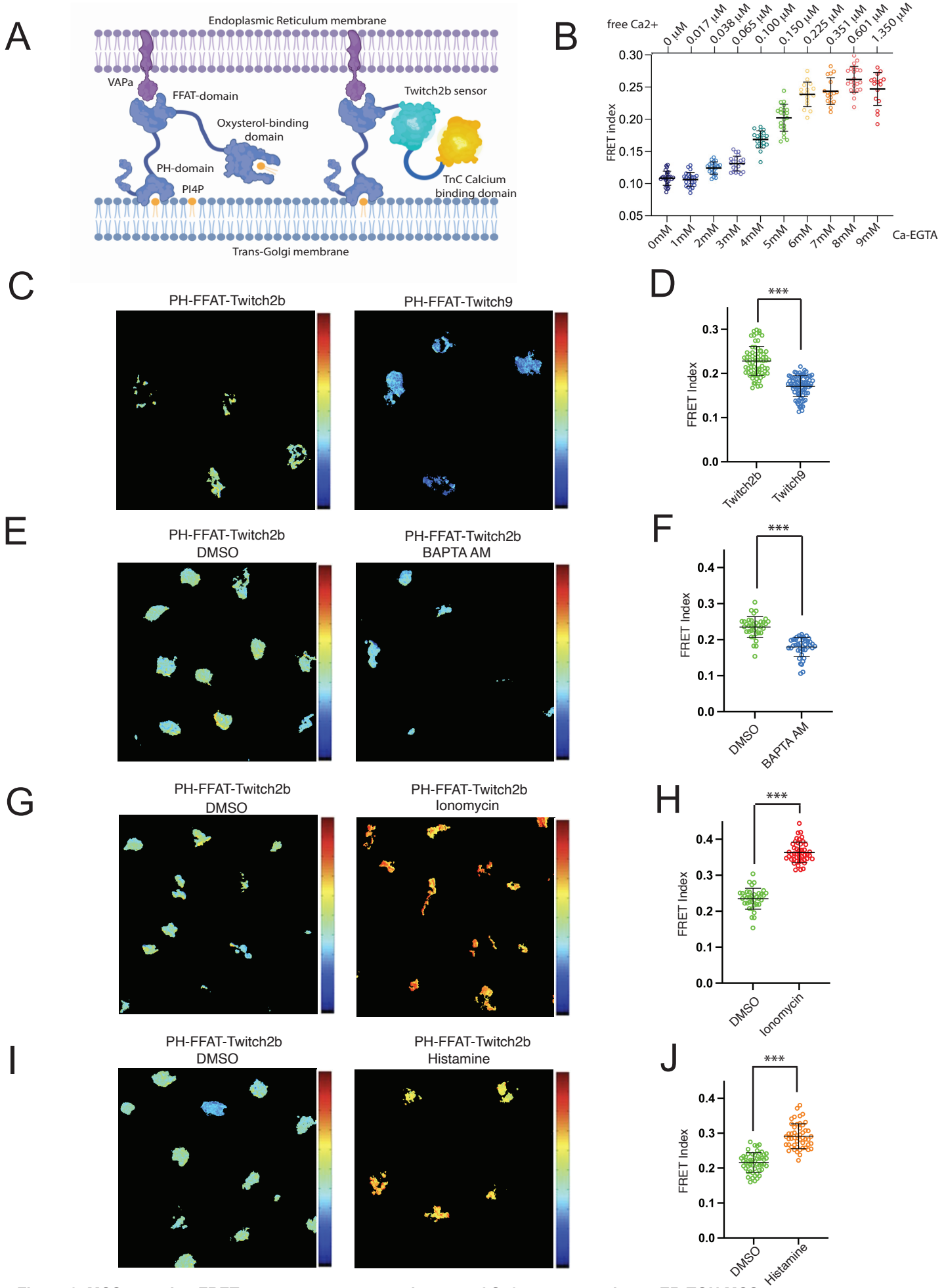

Figure 3. MCS targeting FRET sensor responses to changes of Ca2+ concentration at ER-TGN MCS.
(A) Schematic representation of OSBP and Twitch2b Calcium Sensor targeting Endoplasmic Reticulum-Golgi membrane contact sites. PH domain of OSBP binds to PI4P on the outer leaflet of the TGN membrane and FFAT domain interacts with VAPA on the ER membrane. (B) Calibration curve for Twitch2b sensor performed used buffer with increasing concentration of free Ca2+ ions demonstrating correlation between FRET indices and free Ca2+. (See Materials and Methods for a detailed description). (C) Pseudocolor map of FRET index and dot plot (D) representing FRET indices for PH-FFAT-Twitch2b and PH-FFAT-Twitch9x within Golgi ROI of live cells and at steady state (***p<0.05). (E) Pseudocolor map of FRET index and dot plot (F) representing FRET indices for PH-FFAT-Twitch2b at steady state and treated with 25uM BAPTA-AM for 20 min (***p<0.05). (G) Pseudocolor map of FRET index and dot plot (H) representing FRET indices for PH-FFAT-Twitch2b at steady state and treated with 1uM ionomycin for 20 min (***p<0.05). (I) Pseudocolor map of FRET index and dot plot (J) representing FRET indices for PH-FFAT-Twitch2b at steady state and treated with 1uM Histamine for 2 min (***p<0.05). Pseudocolor bar FRET index value in range 0-0.4.

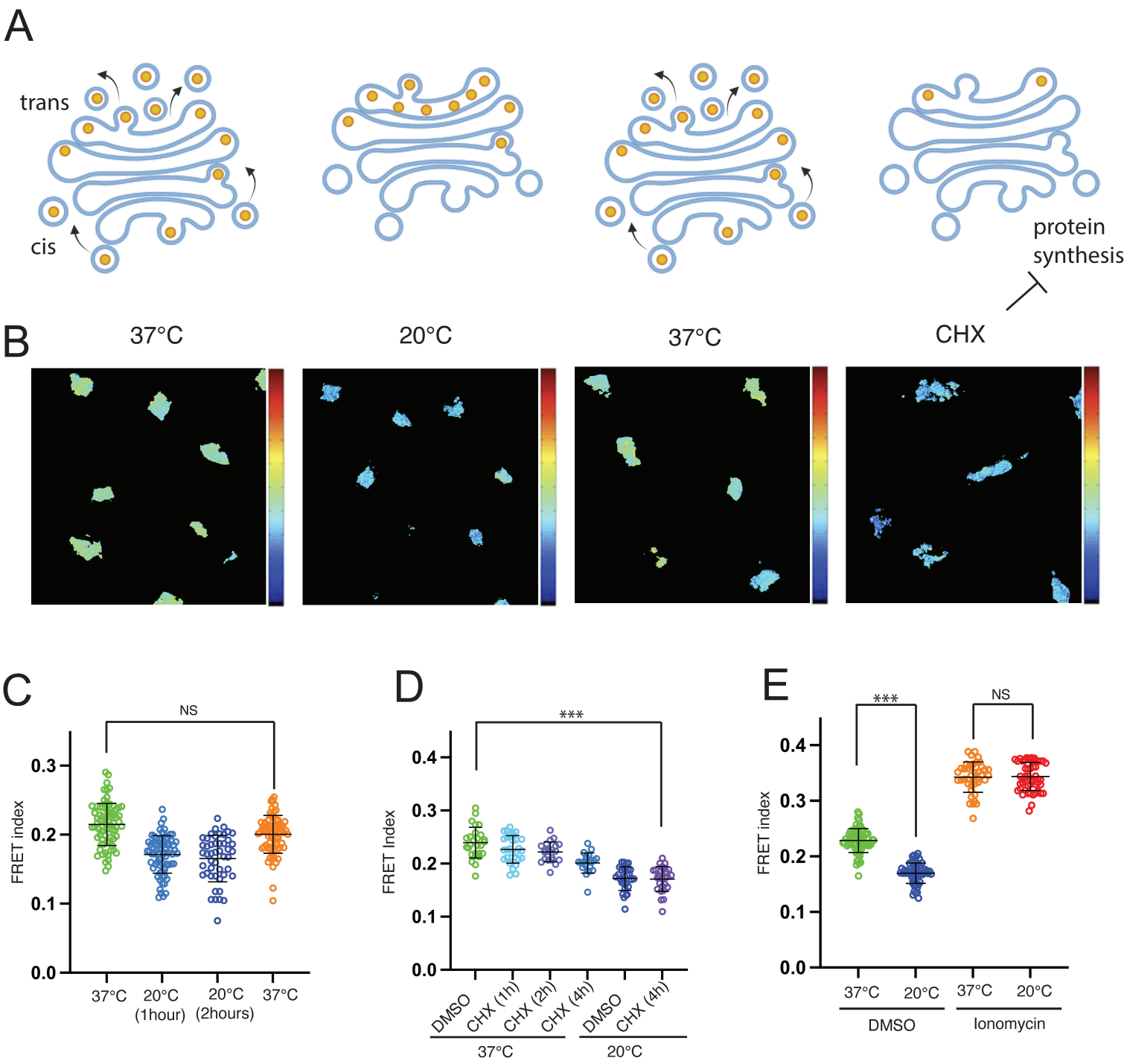

Figure 4. Ca2+ flux at ER-TGN MCS is coupled to protein trafficking
(A) Schematic representation of experiment and effect on protein trafficking in live cells during 20°C block and cycloheximide (CHX) treatment. (B) Pseudocolor maps of FRET index for PH-FFAT-Twitch2b within Golgi ROI of live cells at described above conditions. Pseudocolor bar FRET index value in range 0-0.4. (C) Dot plot representing FRET index for PH-FFAT-Twitch2b at steady state, after 20°C block for 1 and 2 hours and after 10 min recovery at 37°C (***p<0.05). (D) Dot plot representing FRET index for PH-FFAT-Twitch2b at steady state, treated with CHX for 1, 2, 4 hours and after 1h 20°C block. (***p<0.05), (E) Dot plot representing normalized FRET index for PH-FFAT-Twitch2b at steady state, after 1h 20°C block and effect of ionomycin at 37°C and 20°C conditions (***p<0.05).

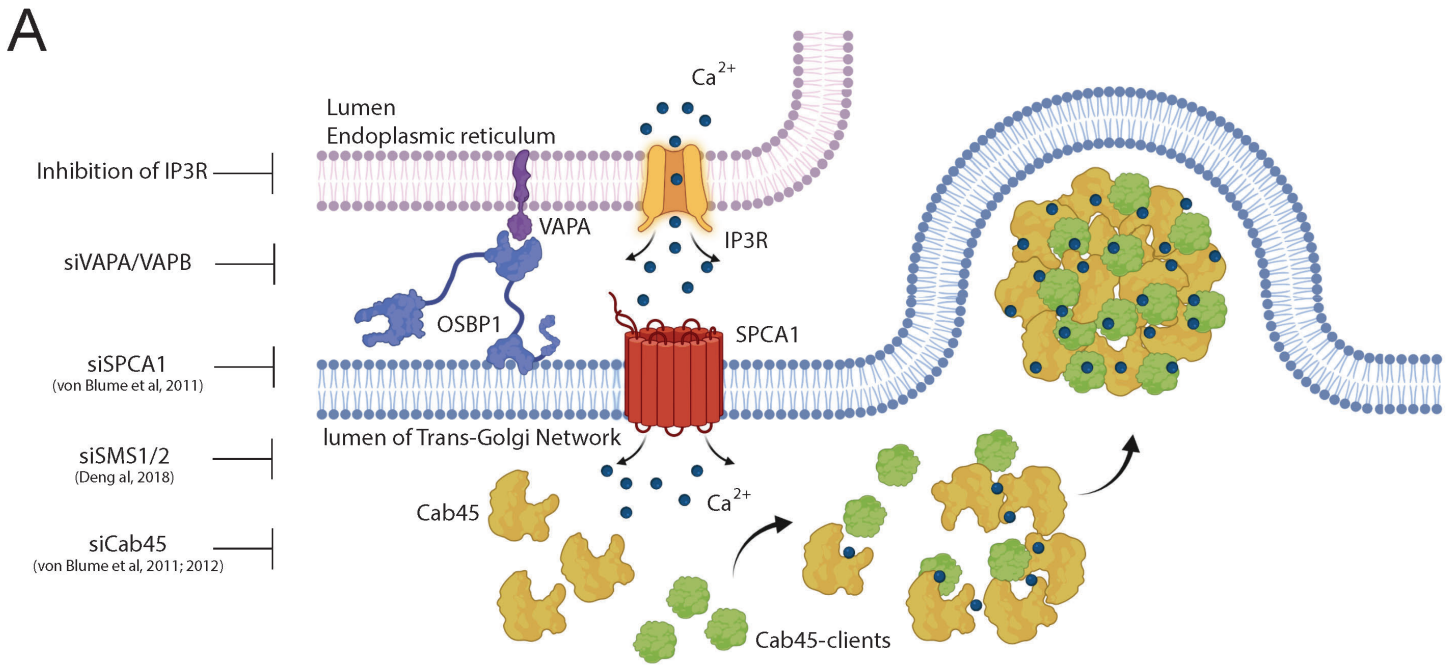

Figure 5A. The model depicting the role of contact sites and IP3R-dependent release of Calcium ions for SPCA1 dependent sorting at TGN.